

# Enhancement of Free Vortex Filament Method for Aerodynamic Loads on Rotor Blades

**Hamidreza Abedi**

Division of Fluid Dynamics,  
Department of Applied Mechanics,  
Chalmers University of Technology,  
Göteborg SE-412 96, Sweden  
e-mail: abedih@chalmers.se

**Lars Davidson**

Division of Fluid Dynamics,  
Department of Applied Mechanics,  
Chalmers University of Technology,  
Göteborg SE-412 96, Sweden  
e-mail: lada@chalmers.se

**Spyros Voutsinas**

Fluid Section,  
School of Mechanical Engineering,  
National Technical University of Athens,  
Athens 15780, Greece  
e-mail: spyros@fluid.mech.ntua.gr

*The aerodynamics of a wind turbine is governed by the flow around the rotor, where the prediction of air loads on rotor blades in different operational conditions and its relation to rotor structural dynamics is one of the most important challenges in wind turbine rotor blade design. Because of the unsteady flow field around wind turbine blades, prediction of aerodynamic loads with high level of accuracy is difficult and increases the uncertainty of load calculations. An in-house vortex lattice free wake (VLFW) code, based on the inviscid, incompressible, and irrotational flow (potential flow), was developed to study the aerodynamic loads. Since it is based on the potential flow, it cannot be used to predict viscous phenomena such as drag and boundary layer separation. Therefore, it must be coupled to tabulated airfoil data to take the viscosity effects into account. Additionally, a dynamic approach must be introduced to modify the aerodynamic coefficients for unsteady operating conditions. This approach, which is called dynamic stall, adjusts the lift, the drag, and the moment coefficients for each blade element on the basis of the two-dimensional (2D) static airfoil data together with the correction for separated flow. Two different turbines, NREL and MEXICO, are used in the simulations. Predicted normal and tangential forces using the VLFW method are compared with the blade element momentum (BEM) method, the GENUVP code, and the MEXICO wind tunnel measurements. The results show that coupling to the 2D static airfoil data improves the load and power predictions while employing the dynamic stall model to take the time-varying operating conditions into consideration is crucial. [DOI: 10.1115/1.4035887]*

## 1 Introduction

The methods for predicting wind turbine performance are similar to propeller and helicopter theories. There are different methods for modeling the aerodynamics of a wind turbine with different levels of complexity and accuracy, such as the BEM theory and solving the Navier–Stokes equations using computational fluid dynamics (CFD). Today, the BEM method is used extensively by wind turbine manufacturers to analyze the aerodynamic performance of a wind turbine. Although it is computationally fast and is easily implemented, it is acceptable only for a certain range of flow conditions [1]. A number of empirical and semi-empirical correction factors have been added to the BEM method in order to increase its application range, such as yaw misalignment, dynamic inflow, finite number of blades, and blade cone angle [2] but they are not relevant to all operating conditions and are often incorrect at high tip speed ratios where wake distortion is significant [3]. Moreover, because of the axisymmetric inflow assumption for the BEM method, it is no longer valid to predict the aerodynamic loads on rotor blades when the wind turbine operates under the yaw condition (because of nonuniform blade loading).

The vortex theory, which is based on the potential, inviscid, and irrotational flow, can also be used to predict the aerodynamic performance of wind turbines. It has been widely used for aerodynamic analysis of airfoils and aircrafts. Although the standard method cannot be used to predict viscous phenomena such as drag

and boundary layer separation, its combination with tabulated airfoil data makes it a powerful tool for the prediction of fluid flow. Compared with the BEM method, the vortex method is able to provide more physical solutions for attached flow conditions using boundary layer corrections, and it is also valid over a wider range of turbine operating conditions. Although it is computationally more expensive than the BEM method, it is still feasible as an engineering method.

In vortex methods, the trailing and shed vortices are modeled by either vortex particles (characterized by a position, a volume, and a strength) [4–6] or vortex filaments [7,8] moving either freely, known as free wake [9–12], or restrictedly by imposing the wake geometry, known as prescribed wake [13,14]. The prescribed wake requires less computational effort than the free wake, but it requires experimental data to be valid for a broad range of operating conditions. The free wake model, which is the most computationally expensive vortex method, is able to predict the wake geometry and loads more accurately than the prescribed wake because of less restrictive assumptions. Therefore, it can be used for load calculations, especially for unsteady flow environment. However, its application is limited to attached flow and it must be linked to tabulated airfoil data to predict the air loads in the presence of the drag and the flow separation.

Additionally, wind turbines always operate in unsteady flow conditions. The unsteadiness sources are classified according to the atmospheric conditions, e.g., wind shear and turbulent inflow together with the turbine structure such as yaw misalignment, rotor tilt, and blade elastic deformation [15], which are considered as perturbations of the local angle of attack and the velocity field. Particularly, unsteady inflow dynamically affects the local angle of attack along the blade due to three-dimensional cross flows and separation. Since the variation in frequency of these sources may

Contributed by the Solar Energy Division of ASME for publication in the JOURNAL OF SOLAR ENERGY ENGINEERING: INCLUDING WIND ENERGY AND BUILDING ENERGY CONSERVATION. Manuscript received February 12, 2016; final manuscript received January 26, 2017; published online March 16, 2017. Assoc. Editor: Douglas Cairns.

be high (rapid transient loads), the quasi-static aerodynamic is no longer valid [16,17]. As a consequence, a dynamic approach must be introduced to modify the aerodynamic coefficients for unsteady operating conditions. This approach, which is called dynamic stall, adjusts the lift, the drag, and the moment coefficients for each blade element on the basis of the 2D static airfoil data together with the correction for separated flow. Furthermore, because of the dynamic stall, the predicted aerodynamic coefficients may result in noticeable differences [16] in comparison with the static ones. A dynamic stall model for the unsteady aerodynamic loads prediction is therefore crucial for the wind turbine technology development.

In this paper, an in-house time-marching VLFW code is used for the simulation where its potential solution is coupled to the tabulated airfoil data for the wind turbine load calculation. In addition, a semi-empirical model, called extended ONERA model, is added to account for the dynamic stall effects. The results of three different load calculation methods, namely standard potential method (potential solution), 2D static airfoil data model (viscous solution), and the dynamic stall model, are compared with the BEM method [1], the GENUVP code,<sup>1</sup> and the MEXICO [18] wind tunnel measurements.<sup>2</sup>

## 2 Theory

Vortex flow theory is based on assuming incompressible ( $\nabla \cdot \mathbf{V} = 0$ ) and irrotational ( $\nabla \times \mathbf{V} = 0$ ) flow at every point except at the origin of the vortex, where the velocity is infinite [19]. A region containing a concentrated amount of vorticity is called a vortex, where a vortex line is defined as a line whose tangent is parallel to the local vorticity vector everywhere. Vortex lines surrounded by a given closed curve make a vortex tube with a strength equal to the circulation  $\Gamma$ . A vortex filament with a strength of  $\Gamma$  is represented as a vortex tube of an infinitesimal cross section with strength  $\Gamma$ .

According to the Helmholtz theorem, an irrotational motion of an inviscid fluid which started from rest remains irrotational. Also, a vortex line cannot end in the fluid. It must form a closed path, end at a solid boundary, or go to infinity; this implies that vorticity can only be generated at solid boundaries. Therefore, a solid surface may be considered as a source of vorticity. Hence, the solid surface in contact with fluid is replaced by a distribution of vorticity.

For an irrotational flow, a velocity potential,  $\Phi$ , can be defined as  $\mathbf{V} = \nabla\Phi$ , where in order to find the velocity field, the Laplace's equation,  $\nabla^2\Phi=0$ , is solved using a proper boundary condition for the velocity on the body and at infinity. In addition, in vortex theory, the vortical structure of a wake can be modeled by either vortex filaments or vortex particles, where a vortex filament is modeled as concentrated vortices along an axis with a singularity at the center.

The velocity induced by a straight vortex filament can be determined by the Biot-Savart law as

$$\mathbf{V}_{\text{ind}} = \frac{\Gamma}{4\pi} \frac{\mathbf{dl} \times \mathbf{r}}{|\mathbf{r}|^3} \quad (1)$$

which can also be written as

$$\mathbf{V}_{\text{ind}} = \frac{\Gamma}{4\pi} \frac{(r_1 + r_2)(\mathbf{r}_1 \times \mathbf{r}_2)}{(r_1 r_2)(r_1 r_2 + \mathbf{r}_1 \cdot \mathbf{r}_2)} \quad (2)$$

where  $\Gamma$  denotes the strength of the vortex filament;  $\mathbf{r}_1$  and  $\mathbf{r}_2$  are the distance vectors from the beginning,  $A$ , and end,  $B$ , of a vortex segment to an arbitrary point  $C$ , respectively (see Fig. 1).

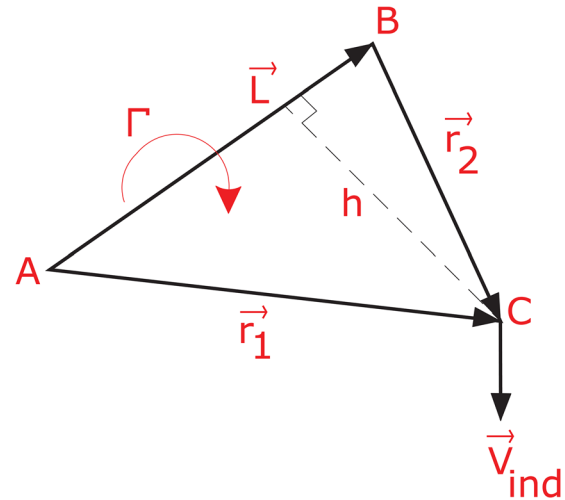


Fig. 1 Schematic for the Biot-Savart law

The Biot-Savart law has a singularity when the point of evaluation ( $C$ ) of induced velocity is located on the vortex filament axis ( $L$ ). Also, when the evaluation point is very near to the vortex filament, there is an unphysically large induced velocity at that point. The remedy is either to use a cut-off radius,  $\delta$  [20], or to use a viscous vortex model with a finite core size by multiplying a factor to remove the singularity [21].

The Biot-Savart law correction based on the viscous vortex model can be made by introducing a finite core size,  $r_c$ , for a vortex filament [22]. In this paper, for simplicity, a constant viscous core size model, which is one of the general approaches using desingularized algebraic profile, is employed for the induced velocity calculations. A general form of a desingularized algebraic swirl-velocity profile for stationary vortices is proposed by Vassitas et al. [23] as

$$V_{\theta}(r) = \frac{\Gamma}{2\pi r} \left( \frac{r^2}{(r_c^{2n} + r^{2n})^{1/n}} \right) \quad (3)$$

where  $r$  and  $n$  are the distance of a vortex segment to an arbitrary point and an integer number, respectively.

Bagai and Leishman [24] suggested the velocity profile based on Eq. (3) for  $n=2$  for rotor tip vortices. Therefore, in order to take into account the effect of the viscous vortex core, a factor of  $K_v$  must be added to the Biot-Savart law as [24]

$$\mathbf{V}_{\text{ind}} = K_v \frac{\Gamma}{4\pi} \frac{(r_1 + r_2)(\mathbf{r}_1 \times \mathbf{r}_2)}{(r_1 r_2)(r_1 r_2 + \mathbf{r}_1 \cdot \mathbf{r}_2)} \quad (4)$$

where

$$K_v = \frac{h^2}{(r_c^{2n} + h^{2n})^{1/n}} \quad (5)$$

and  $h$  is defined as the perpendicular distance of the evaluation point (see Fig. 1). Factor  $K_v$  desingularizes the Biot-Savart equation when the evaluation point distance tends to zero and prevents a high induced velocity in the vicinity region of the vortex core radius.

## 3 Model

**3.1 Assumptions.** In this study, as a first effort to evaluate the load calculation methods (see Sec. 3.3), the upstream flow is set to be uniform, both in time and space. For the nonyawed flow, it is perpendicular to the rotor plane whereas for the yawed flow it

<sup>1</sup>GENUVP is an unsteady flow solver based on vortex blob approximations developed for rotor systems by National Technical University of Athens.

<sup>2</sup>The MEXICO wind turbine measurements were carried out in 2006 in the Large Scale Low Speed Facility (LLF) of the German Dutch Wind Tunnel (DNW).

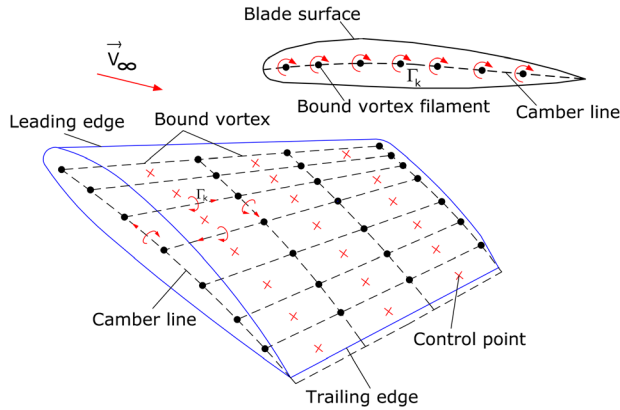


Fig. 2 Lifting surface and vortex panels construction

is not (it deviates from the rotating axis). It should be noted that a yaw misalignment makes the inflow unsteady even if the upstream flow does not change in time and space (steady state).

However, the VLFW code can handle both uniform or nonuniform flow (varying both in time and space). The blades are assumed to be rigid, i.e., the elastic effects of the blades are neglected.

**3.2 Vortex Lattice Free Wake.** The vortex lattice method (Fig. 3) is based on the thin lifting surface theory of vortex ring elements [25], in which the blade surface is replaced by vortex panels that are constructed based on the airfoil camber line of each blade section (see Fig. 2). The solution of Laplace's equation with a proper boundary condition gives the flow around the blade resulting in an aerodynamic load calculation, generating power and thrust of the wind turbine. To take the blade surface curvature into account, the lifting surface is divided into a number of panels, both in the chordwise and spanwise directions, where each panel contains a vortex ring with strength  $\Gamma_{ij}$  in which  $i$  and  $j$  indicate panel indices in the chordwise and spanwise directions, respectively. The strength of each blade bound vortex ring element,  $\Gamma_{ij}$ , is assumed to be constant, and the positive circulation is defined on the basis of the right-hand rotation rule.

In order to fulfill the 2D Kutta condition (which can be expressed as  $\gamma_{T.E.} = 0$  in terms of the strength of the vortex sheet

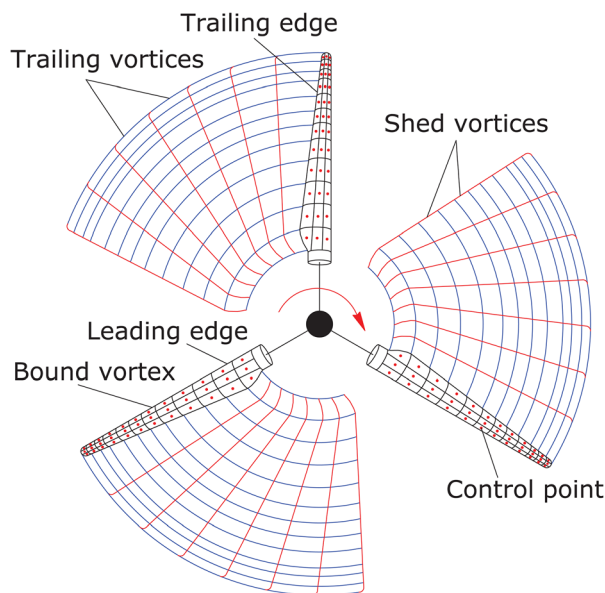


Fig. 3 Schematic of vortex lattice free wake

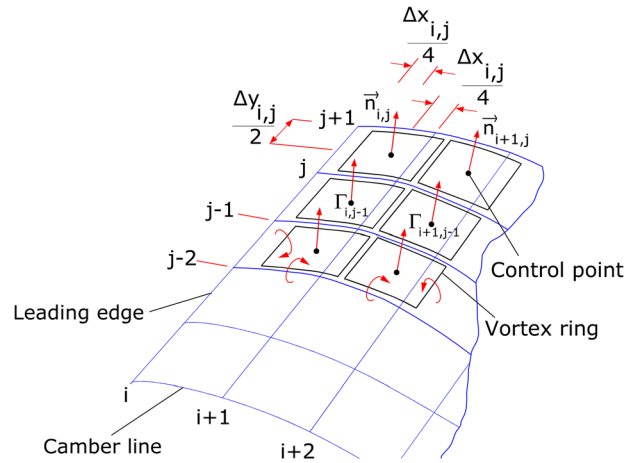


Fig. 4 Numbering procedure

where the T.E. subscripts denotes the trailing edge), the leading segment of a vortex ring is located at 1/4 of the panel length (see Fig. 4). The control point of each panel is located at 3/4 of the panel length, meaning that the control point is placed at the center of the panel's vortex ring.

The wake elements which induce a velocity field around the rotor blades are modeled as vortex ring elements, and they are trailed and shed from the trailing edge based on a time-marching method. To satisfy the 3D trailing edge condition for each spanwise section, the strength of the trailing vortex wake rings must be equal to the last vortex ring row in the chordwise direction ( $\Gamma_{T.E.} = \Gamma_{wake}$ ). This mechanism allows that the blade bound vorticity is transformed into free wake vortices.

To find the blade bound vortices' strength at each time step, the flow tangency condition at each blade's control point must be specified by establishing a system of equations. The velocity components at each blade control point include the free stream ( $\mathbf{V}_\infty$ ), rotational ( $\Omega\mathbf{r}$ ), blade vortex rings self-induced ( $\mathbf{V}_{ind, bound}$ ), and wake induced ( $\mathbf{V}_{ind, wake}$ ) velocities. The blade-induced component is known as influence coefficient  $a_{ij}$  and is defined as the induced velocity of a  $j$ th blade vortex ring with a strength equal to one on the  $i$ th blade control point given by

$$a_{ij} = (\mathbf{V}_{ind, bound})_{ij} \cdot \mathbf{n}_i \quad (6)$$

If the blade is assumed to be rigid, then the influence coefficients are constant at each time step, which means that the left-hand side of the equation system is computed only once. However, if the blade is modeled as a flexible blade, they must be calculated at each time step. Since the wind and rotational velocities are known during the wind turbine operation, they are transferred to the right-hand side of the equation system. In addition, at each time step, the strength of the wake vortex panels is known from the previous time step, so the induced velocity contribution by the wake panels is also transferred to the right-hand side. Therefore, the system of equations can be expressed as

$$\begin{pmatrix} a_{11} & a_{12} & \cdots & a_{1m} \\ a_{21} & a_{22} & \cdots & a_{2m} \\ \vdots & \vdots & \ddots & \vdots \\ a_{m1} & a_{m2} & \cdots & a_{mm} \end{pmatrix} \begin{pmatrix} \Gamma_1 \\ \Gamma_2 \\ \vdots \\ \Gamma_m \end{pmatrix} = \begin{pmatrix} \text{RHS}_1 \\ \text{RHS}_2 \\ \vdots \\ \text{RHS}_m \end{pmatrix} \quad (7)$$

where  $m$  is defined as  $m = MN$  for a blade with  $M$  spanwise and  $N$  chordwise panels and the right-hand side is computed as

$$\text{RHS}_k = -(\mathbf{V}_\infty + \Omega\mathbf{r} + \mathbf{V}_{ind, wake})_k \cdot \mathbf{n}_k \quad (8)$$

The blade bound vortex strength ( $\Gamma_{ij}$ ) is calculated by solving Eq. (7) at each time step. At the first time step (see Figs. 5 and 6),

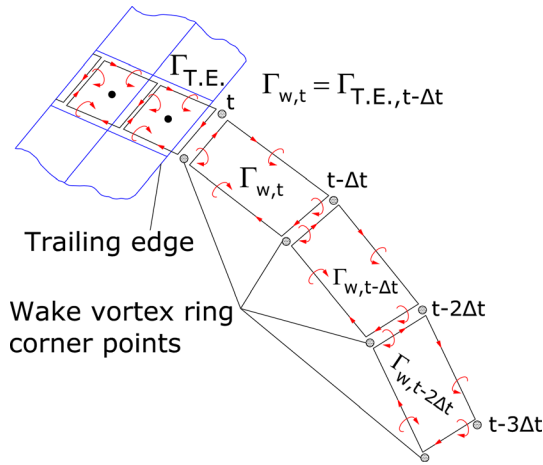


Fig. 5 Schematic of generation and moving of wake panels at each time step

there are no free wake elements. At the second time step (see Figs. 5 and 7), when the blade is rotating, the first wake panels are shed. Their strength is equal to the bound vortex circulation of the last row of the blade vortex ring elements (Kutta condition), located at the trailing edge, at the previous time step (see Fig. 7), which means that  $\Gamma_{W_2} = \Gamma_{T.E.,t_1}$ , where the  $W$  and  $T.E.$  subscripts represent the wake and the trailing edge, respectively. At the second time step, the strength of the blade bound vortex rings is calculated by specifying the flow tangency boundary condition where, in addition to the blade vortex ring elements, the contribution of the first row of the wake panels is considered.

This methodology is repeated, and vortex wake elements are trailed and shed at each time step, where their strengths remain constant (Kelvin theorem). In addition, the corner points of vortex wake elements are moved based on the governing equation for the wake geometry given by

$$\frac{d\mathbf{r}}{dt} = \mathbf{V}_{\text{tot}}(\mathbf{r}) \quad \mathbf{r}(t=0) = \mathbf{r}_0 \quad (9)$$

where  $\mathbf{r}$ ,  $\mathbf{V}_{\text{tot}}$ , and  $t$  denote the position vector of a Lagrangian marker, the total velocity field, and time, respectively. The total velocity field, expressed in the rotating reference frame, i.e.,  $\mathbf{V}_{\text{rot}} = 0$ , can be written as

$$\mathbf{V}_{\text{tot}} = \mathbf{V}_{\infty} + \mathbf{V}_{\text{ind,blade}} + \mathbf{V}_{\text{ind,wake}} \quad (10)$$

including the wind velocity and the induced velocity by all blades and wake vortex rings.

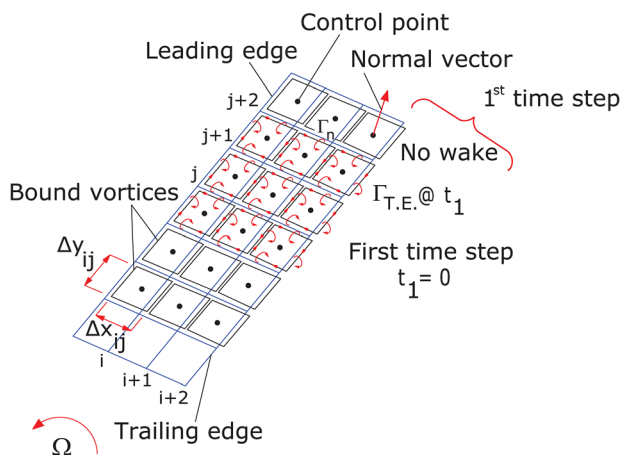


Fig. 6 Schematic of wake evolution at the first time step

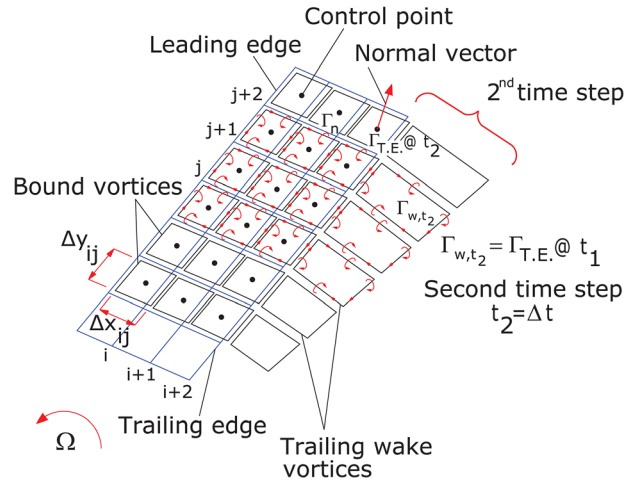


Fig. 7 Schematic of wake evolution at the second time step

Different numerical schemes may be used for Eq. (9) such as the explicit Euler method, the implicit method, Adams–Bashforth method, and the Predictor–Corrector method. The numerical integration scheme must be considered in terms of the accuracy, stability, and computational efficiency. Here, the first-order Euler explicit method is used as

$$\mathbf{r}_{t+1} = \mathbf{r}_t + \mathbf{V}_{\text{tot}}(\mathbf{r}_t)\Delta t \quad (11)$$

where  $\mathbf{V}_{\text{tot}}$  is taken at the old time step.

**3.3 Load Calculation.** In the vortex flow, the only force acting on the rotor blades is the lift force, which can be calculated either by the Kutta–Jukowski theory or by the Bernoulli equation where the viscous effects such as the skin friction and the flow separation are not included. Therefore, in order to take into account the viscous effects and the flow separation, the inviscid lift force must be combined with the aerodynamic coefficients through the tabulated airfoil data along with the dynamic stall model to take the unsteady effects into account.

The currently developed model (VLFW) is based on the thin lifting surface theory of vortex ring elements, where the body is part of the flow domain. Therefore, the effective angle of attack is calculated by projecting the lift force acting on rotor blades into the normal and tangential directions with respect to the rotor plane. In general, the predicted angle of attack computed on the basis of the potential flow solution (i.e., the lifting surface theory) is always greater than that calculated by the viscous flow. Therefore, it cannot be directly used as entry to look up the tabulated airfoil data to provide the aerodynamic coefficients. This leads us to modify the predicted angle of attack by introducing a method called the 2D static airfoil data method (viscous solution).

In the 2D static airfoil data method, the new angle of attack is calculated by using the tabulated airfoil data where it is directly connected to both the tabulated airfoil data and the potential solution parameter ( $\Gamma$ ). This angle of attack is used as the entry to look-up the airfoil table and then we are able to calculate the lift, drag, and moment coefficients giving the lift and drag forces for each blade element. It is worth noting that both the standard potential method and 2D static airfoil data method are based on the quasi-static assumption.

In the fully unsteady condition, since the lift, drag, and moment coefficients are not following the tabulated airfoil data curve (see Appendix), they should be corrected and this is done by employing a dynamic stall model. Generally, the aim of the dynamic stall model is to correct the aerodynamic coefficients under the different time-dependent events which were described in the introduction. Hence, in case of uniform, steady inflow condition and in the

absence of the yaw misalignment, the rotor tilt, and the blade aeroelastic motion, it is not necessary to use the dynamic stall model.

**3.3.1 The Standard Potential Method.** In the VLFW method, when the positions of all Lagrangian markers are calculated at each time step, we are able to compute the velocity field around the rotor blade where, as a consequence, the lift force can be calculated according to the Kutta–Jukowski theorem. The differential steady-state form of the Kutta–Jukowski theorem reads

$$d\mathbf{L} = \rho \mathbf{V}_{\text{tot}} \times \Gamma d\mathbf{l} \quad (12)$$

where  $\rho$ ,  $\mathbf{V}_{\text{tot}}$ ,  $\Gamma$  and  $d\mathbf{l}$  denote the air density, total velocity vector, vortex filament strength, and vortex filament length vector, respectively.

The Kutta–Jukowski theorem is applied at the midpoint of the front edge of each blade vortex ring and gives the potential lift force where the lift force of each spanwise blade section is calculated by summing up the lift force of all panels along the chord. The lift force for each blade panel is computed using the general form of the Kutta–Jukowski theorem given by

$$\mathbf{L}_{i,j} = \rho \mathbf{V}_{\text{tot},i,j} \times (\Gamma_{i,j} - \Gamma_{i-1,j}) \Delta \mathbf{y}_{i,j} + \left( \rho A_{i,j} \frac{\Delta \Gamma_{i,j}}{\Delta t} \mathbf{n}_{i,j} \right) \quad (13)$$

where  $\Delta \mathbf{y}_{i,j}$ ,  $A_{i,j}$ ,  $\Delta \Gamma_{i,j}/\Delta t$ , and  $\mathbf{n}_{i,j}$  denote the width vector of a blade vortex panel in the chordwise direction, blade vortex panel area, time-gradient of circulation, and unit vector normal to the vortex panel in which  $i$  and  $j$  indicate panel indices in the chordwise and spanwise directions, respectively. Moreover,  $\mathbf{V}_{\text{tot},i,j}$  is computed as

$$\mathbf{V}_{\text{tot},i,j} = \mathbf{V}_{\infty,i,j} + \Omega \mathbf{r}_j + \mathbf{V}_{\text{ind,wake},i,j} + \mathbf{V}_{\text{ind,bound},i,j} \quad (14)$$

The second term in Eq. (13) is the unsteady term which may be neglected for the steady-state computations. For the blade panels adjacent to the leading edge, Eq. (13) can be written as

$$\mathbf{L}_{1,j} = \rho \mathbf{V}_{\text{tot},1,j} \times \Gamma_{1,j} \Delta \mathbf{y}_{1,j} + \left( \rho A_{1,j} \frac{\Delta \Gamma_{1,j}}{\Delta t} \mathbf{n}_{1,j} \right) \quad (15)$$

The total lift of each blade section in the spanwise direction is obtained as

$$\mathbf{L}_j = \sum_{i=1}^N \mathbf{L}_{i,j} \quad (16)$$

where  $N$  denotes the number of chordwise sections. Decomposition of the lift force for each blade spanwise section into the normal and tangential directions with respect to the rotor plane (see Fig. 8) gives the effective potential angle of attack for each section

$$\alpha = \tan^{-1}(F_t/F_n) - \theta_t - \theta_p \quad (17)$$

where  $\alpha$ ,  $F_t$ ,  $F_n$ ,  $\theta_t$ , and  $\theta_p$  represent the angle of attack, tangential force, normal force, blade section twist, and blade pitch, respectively.

**3.3.2 Two-Dimensional Static Airfoil Data Method.** In potential flow, the lift coefficient is expressed by the thin airfoil theory, which is a linear function of angle of attack with constant slope equal to  $2\pi$ . This means that for the thick airfoil, commonly used in wind turbine blades, the thin airfoil theory is no longer valid. In addition, because of this linear relation of the lift coefficient and the angle of attack, this assumption gives the higher lift the higher the angle of attack. Hence, considerable lift reduction due to flow separation at higher angles of attack cannot be predicted. In other

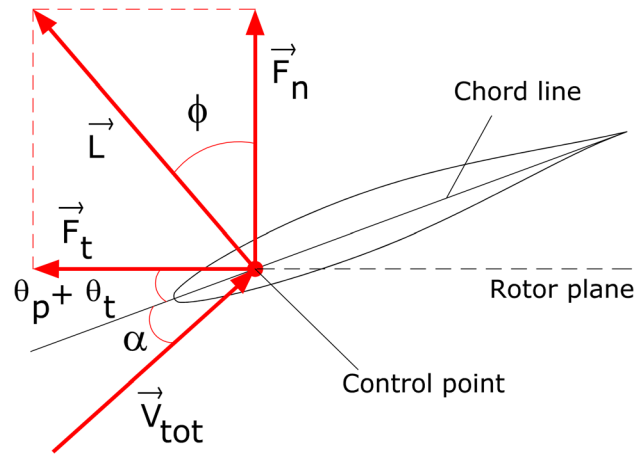


Fig. 8 Potential load decomposition

words, the application of thin airfoil theory is limited to attached flow and it must be linked to tabulated airfoil data to predict air loads in the presence of drag and flow separation. Coupling the thin airfoil theory (standard potential method) to the tabulated airfoil data for wind turbine load calculation is done by employing the 2D static airfoil data method as described here.

According to the Kutta–Jukowski theory, the magnitude of the lift force per unit spanwise length,  $L'$ , is proportional to the circulation,  $\Gamma$ , and it is given by

$$L' = \rho V_{\text{tot}} \Gamma \quad (18)$$

where  $\rho$ ,  $V_{\text{tot}}$  denote the air density and the total velocity magnitude, respectively. The circulation for each spanwise section is equal to the bound vortex circulation of the last row vortex ring element, located at the trailing edge. In addition, in the linear airfoil theory, the lift coefficient is expressed by

$$C_L = m(\alpha - \alpha_0) \quad (19)$$

where  $m = 2\pi$ ,  $\alpha$  and  $\alpha_0$  indicate the slope, the angle of attack, and the zero-lift angle of attack, respectively. The lift coefficient is generally defined as

$$C_L = \frac{L'}{0.5\rho V_{\text{tot}}^2 c} \quad (20)$$

where  $c$  denotes the airfoil chord length. Combination of Eqs. (18)–(20) gives the modified angle of attack as

$$\alpha = \frac{2\Gamma}{mV_{\text{tot}}c} + \alpha_0 \quad (21)$$

For an arbitrary airfoil, both  $m$  and  $\alpha_0$  are determined according to the  $C_L$  versus  $\alpha$  curve where the constant lift coefficient slope,  $m$ , is computed over the linear region (attached flow). The modified angle of attack based on the Eq. (21) is used as entry to calculate the lift, the drag, and the moment coefficients through the tabulated airfoil data. As a result, the lift and drag forces are computed for each blade element in the spanwise direction which consequently gives the tangential and normal forces acting on the rotor blade (see Fig. 9).

**3.3.3 Dynamic Stall Method.** The semi-empirical dynamic stall model, called the extended ONERA, is used to predict the unsteady lift, drag, and moment coefficients for each blade spanwise section based on 2D static airfoil data. In this model, the unsteady airfoil coefficients are described by a set of differential equations including the excitation and the response variables,

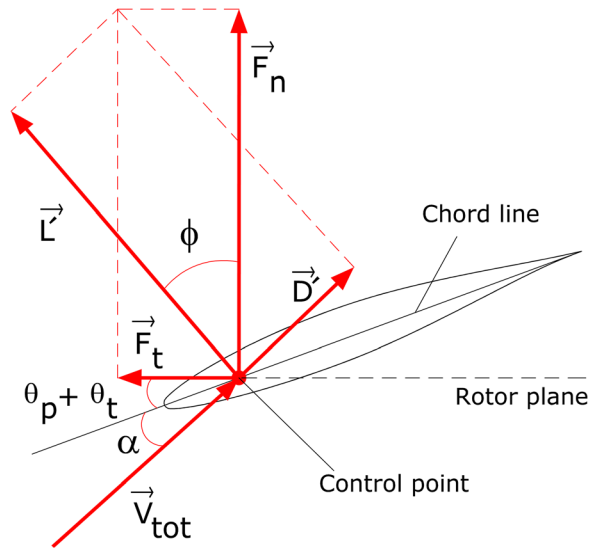


Fig. 9 Viscous load decomposition

where they are applied separately for both the attached and separated flows.

In the extended ONERA model, the lift ( $L'$ ) and the drag ( $D'$ ) forces per unit spanwise length are written as

$$L' = \frac{\rho c}{2} \left[ V_{\text{tot}} (\Gamma_{1L} + \Gamma_{2L}) + \frac{S_{LC}}{2} \dot{W}_0 + \frac{K_{LC}}{2} \dot{W}_1 \right] \quad (22)$$

and

$$D' = \frac{\rho c}{2} \left[ V_{\text{tot}}^2 C_{D,\text{Lin}} + \frac{\sigma_{DC}}{2} \dot{W}_0 + V_{\text{tot}} \Gamma_{2D} \right] \quad (23)$$

where the symbol  $(\dot{\phantom{x}})$ ,  $\rho$ ,  $c$ ,  $V_{\text{tot}}$ ,  $\Gamma_{1L}$ ,  $\Gamma_{2L}$ ,  $W_0$ ,  $W_1$ ,  $\Gamma_{2D}$ , and  $C_{D,\text{Lin}}$  denote the derivation with respect to time, air density, blade element chord length, total velocity, linear circulation related to the attached flow lift, nonlinear circulation related to the separated flow lift, total velocity component perpendicular to the sectional

chord, rotational velocity of the blade section due to the pitching oscillation, nonlinear circulation related to the separated flow drag, and linear drag coefficient (see Fig. 25), respectively. It should be noted that different circulation terms in Eqs. (22) and (23) are the circulation divided by half chord length. For detailed description of other coefficients in Eqs. (22) and (23), see Appendix.

## 4 Results

To validate different load calculation methods implemented in the VLFW code, the NREL 5-MW [26] and MEXICO [18] turbines are used in the simulations. For the NREL 5-MW machine, in addition to the power and thrust curves, the angle of attack and tangential force along the rotor blade are studied and they are compared with the BEM method and the GENUVP code. For the MEXICO turbine, two different steady inflow conditions (with and without yaw misalignment) are employed in the VLFW simulations. The tangential and normal forces acting on the rotor blades are compared with the existing experimental data.

**4.1 NREL-5 MW Turbine.** Table 1 shows the operating conditions in which the simulations have been done for the NREL 5-MW reference wind turbine. Among these operating conditions, three cases based on the low, middle, and high freestream velocities were chosen for further studies. In the vortex method simulations made with VLFW code, the blade is discretized with  $M = 24$  spanwise sections (see Fig. 10) and  $N = 8$  equally spaced chordwise sections. Because of the large circulation gradients ( $d\Gamma/dr$ ) near the tip of the rotor blade, the cosine rule for the blade spanwise segmentation [2] is used where the blade elements are distributed at equi-angle increments in the radial direction resulting in a fine tip resolution. Increments of 10 deg are employed for the wake segmentation and the wake length is truncated after four rotor diameters [27]. The free stream is assumed to be uniform, steady, and perpendicular to the rotor plane. The vortex core size is one of the most important parameters in the free vortex wake models which affects the vortex roll-up and wake development. Different parameters may affect the vortex core radius such as operating condition and blade radius. Choosing a large vortex core size delays the vortex roll-up. On the other hand, a small vortex core size does not significantly affect the tip vortex roll-up, but it makes the trailing wake vortices to deflect earlier which

Table 1 NREL 5-MW turbine operating conditions

Case No.	1	2	3	4	5	6	7	8	9	10	11
$V_{\infty}$ (m/s)	5	6	7	8	9	10	11	12	13	14	15
$\Omega$ (rad/s)	0.627	0.753	0.878	1.003	1.129	1.255	1.267	1.267	1.267	1.267	1.267
$\theta_p$ (deg)	0.0	0.0	0.0	0.0	0.0	0.0	0.0	4.0	6.65	8.70	10.46

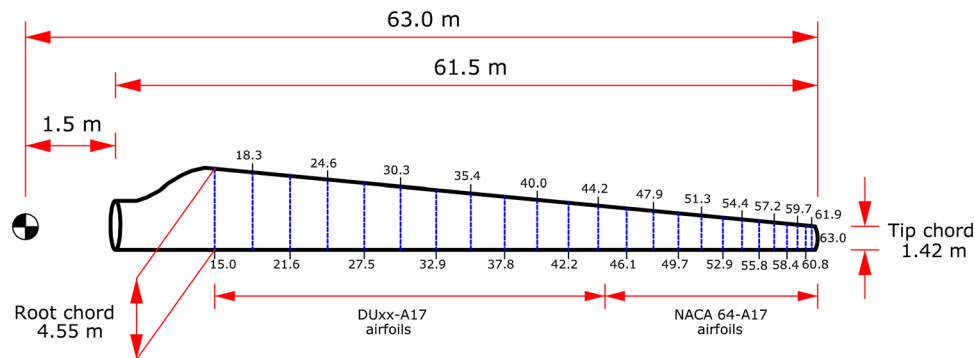
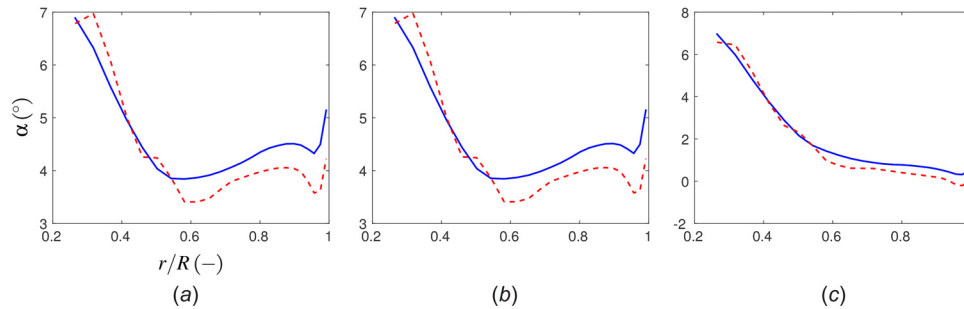
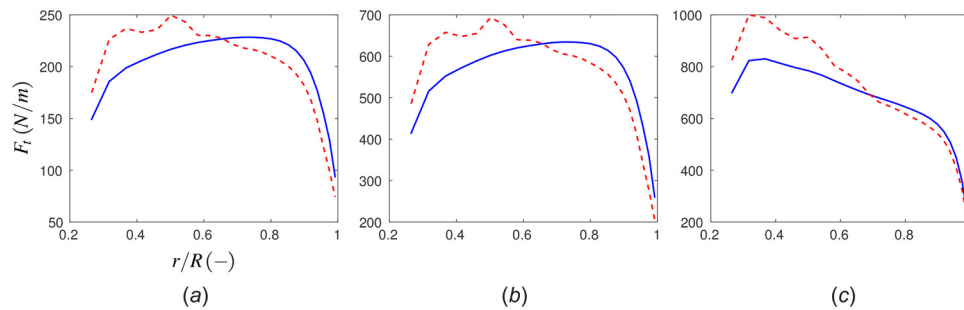


Fig. 10 Radial distribution of blade elements for NREL-5 MW turbine



**Fig. 11** Distribution of angle of attack along the blade for the NREL turbine: (a) case 2, (b) case 6, and (c) case 10; — potential and -- viscous



**Fig. 12** Distribution of tangential force along the blade for the NREL turbine: (a) case 2, (b) case 6, and (c) case 10; — potential and -- viscous

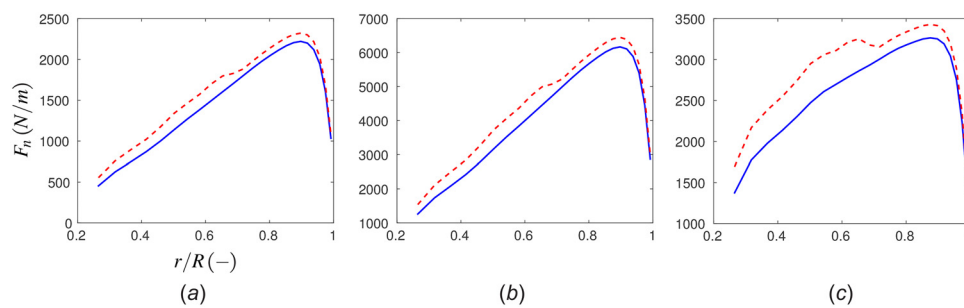


**Fig. 13** Distribution of normal force along the blade for the NREL turbine: (a) case 2, (b) case 6, and (c) case 10; — potential and -- viscous

increases the wake instability. For the NREL-5 MW turbine, it is assumed that the wake vortex filament core radius is constant and is equal to 1.0 m.

Figure 11 shows the angle of attack along the blade. As can be seen, the potential angle of attack is greater than the viscous one for  $r/R > 0.5$ , which is consistent with the higher power production, predicted by the potential solution. The blade of the NREL-5 MW machine is constructed by different airfoil profiles [26]. Computing the lift coefficient slope in the linear region (attached flow) for each airfoil profile shows that this slope is larger than the slope for the thin airfoil theory ( $m = 2\pi$ ). Equation (21) implies that the larger the lift coefficient slope ( $m$ ), the lower the angle of attack. Therefore, the modification of the potential angle of attack by coupling to the 2D airfoil data influences aerodynamic loads and generated power.

Figure 12 shows the tangential force along the blade with respect to the rotor plane. The predicted tangential force by the potential solution is significantly larger near the blade tip making more power in comparison with the viscous solution. The tangential force calculated by the viscous solution gives larger values than the potential solution near the blade root region. This difference between the potential and viscous solutions for the tangential

force close to the blade root increases even more for higher wind velocity where the turbine is pitch regulated to prevent the turbine operating above the rated power.

Figure 13 shows the normal force along the blade with respect to the rotor plane. Contrary to the tangential force, the viscous solution predicts larger normal forces than the potential solution. The reason for this difference is the drag force, which is only taken into account the viscous solution. Furthermore, for higher wind velocity where the turbine is pitch regulated, the normal force along the blade decreases, which reduces the turbine's thrust coefficient (see Fig. 14 (right)).

The power and thrust curves are obtained by integrating the tangential and normal forces along the blade, respectively. Therefore, the comparison between the different methods was only performed for the power and thrust curves. As seen in Fig. 14 (left), there is a good quantitative agreement among the different VLFW load calculation methods. For the wind velocity less than 11 m/s where the turbine is not pitch regulated, the difference between the potential and viscous solutions is negligible. But, this difference increases for wind velocity higher than 11 m/s (pitch regulated zone), showing the necessity to modify the standard potential method using the tabulated airfoil data. Moreover,

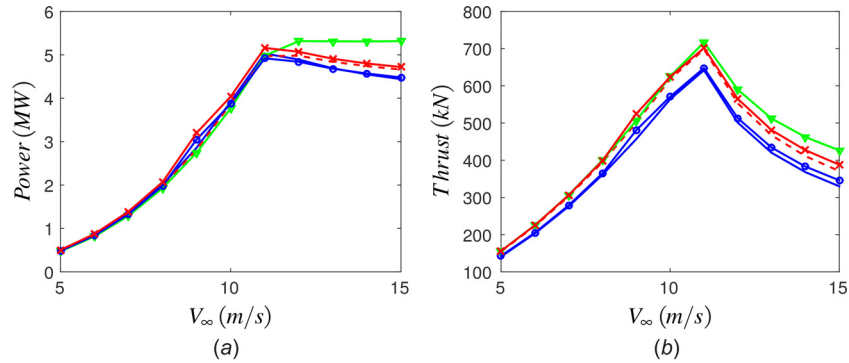


Fig. 14 (a) power and (b) thrust curves for the NREL turbine; — VLFW potential, -- VLFW viscous, -- BEM, — ° — GENUVP potential, and — x — GENUVP viscous

Table 2 MEXICO turbine operating conditions

Item	Case	$V_\infty$ (m/s)	$\Omega$ (rad/s)	$\rho$ (kg/m <sup>3</sup> )	$\theta_p$ (°)	$\chi$ (°)
No yaw	1	10.01	44.45	1.245	-2.3	0
	2	14.93	44.45	1.246	-2.3	0
	3	23.96	44.45	1.236	-2.3	0
Yaw	1	14.99	44.45	1.237	-2.3	30

Fig. 14 (right) displays the thrust curve for the 5-MW NREL turbine. By increasing the upstream flow, the wind turbine thrust linearly increases and it suddenly drops at freestream velocity of 11 m/s when the blade pitch angle is increased. As observed, the different load calculation methods approximately provide similar results, but there are distinctive differences between them because of the unsteady environment which will be discussed in Sec. 4.2.

**4.2 MEXICO Turbine.** The 3-bladed MEXICO wind turbine [18] is used in the simulations. The radius of the MEXICO turbine's blades is 2.05 m. The simulations are performed for both nonyawed and yawed inflow conditions. Table 2 shows the operating conditions at which the MEXICO measurements have been done.  $V_\infty$ ,  $\Omega$ ,  $\rho$ ,  $\theta_p$ , and  $\chi$  denote the free stream velocity, rotational velocity, air density, blade pitch angle, and yaw misalignment, respectively. The MEXICO turbine's rotational direction is clockwise and the positive yaw angle is defined as clockwise with respect to the radial (y) axis. Moreover, in the VLFW simulation, the turbine's nacelle is not modeled.

In the VLFW code, the blade is discretized with  $M=24$  spanwise sections (see Fig. 15) and  $N=10$  equally spaced chordwise sections. The same methodology is applied for the blade, wake segmentation, and vortex filament core radius as described in Sec.

4.1 for the NREL 5-MW turbine. It is assumed that the wake vortex filament core radius is constant and is equal to 0.1 m. Moreover, for the nonyawed flow, the free stream is assumed to be uniform, steady, and perpendicular to the rotor plane and for the yawed flow, it is assumed to be uniform and steady deviated +30 deg with respect to the rotor axis (z). For the yawed flow simulation, all coefficients in the dynamic stall model are taken according to the flat plate and the mean profile values (see Appendix).

**4.2.1 Nonyawed Flow.** For the nonyawed inflow, the normal and axial forces along the rotor for three different operating conditions (see Table 2) are compared against the MEXICO experiment. As observed in Fig. 16, both the standard potential method (potential solution) and the 2D static airfoil data method (viscous solution) overpredict the normal force with respect to the experiments. However, there is a rather good agreement between the simulation (especially for the viscous solution) and the measurement. The difference between the potential and viscous solutions increases by increasing the freestream velocity. This means that for the higher freestream velocities, the viscous phenomena such as flow separation and stall condition increase the flow complexity around the blade making the potential assumption less accurate. The discrepancy between the potential and viscous solutions indicates that the flow separation occurs for the blade root region (inboard positions) even for the lower wind velocities and it moves toward the blade tip region (outboard positions) for higher wind velocities.

Figure 17 displays the tangential force along the blade compared to the measurements where a qualitative agreement between the simulation and measurement is seen. Like the normal force, the potential solution shows the same trend as the experimental results; the higher the wind velocity, the larger the forces acting on the rotor. However, including the viscosity effects using the tabulated airfoil data in the viscous solution gives a better

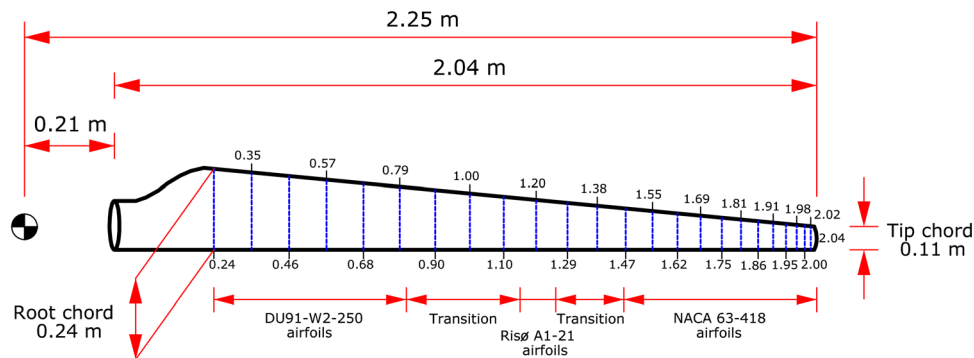
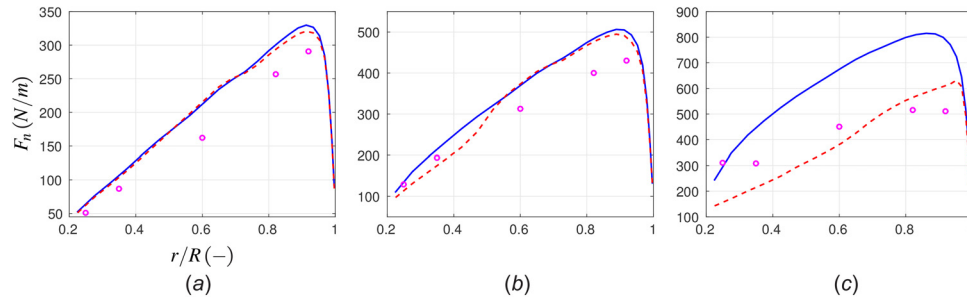
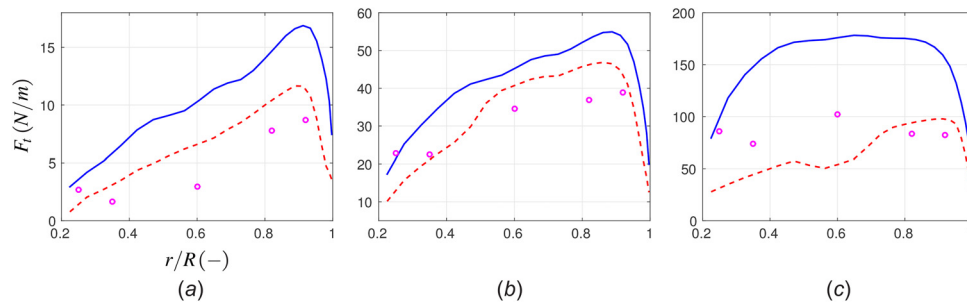


Fig. 15 Radial distribution of blade elements for MEXICO turbine



**Fig. 16** Distribution of normal force along the MEXICO turbine's blade, nonyawed flow: (a) case 1, (b) case 2, and (c) case 3, — potential, -- viscous, and  $\circ$  experiment



**Fig. 17** Distribution of tangential force along the MEXICO turbine's blade, nonyawed flow: (a) case 1, (b) case 2 and (c) case 3, — potential, -- viscous, and  $\circ$  experiment

prediction compared with the potential solution. As explained in Ref. [16], the centrifugal and Coriolis forces acting on the boundary layer increases the maximum lift coefficient (especially for the blade root region) and delays the flow separation and stall as well. Therefore, the larger tangential force given by the experiments for the inboard positions (compared to the viscous solution) may be due to the centrifugal and Coriolis forces which are not considered in the tabulated airfoil data.

**4.2.2 Yawed Flow.** For the yawed flow, the aerodynamic forces normal and parallel to the local chord as a function of azimuthal position for the five radial stations along blade 1 are compared against measurement data. These five stations are located at  $0.25R$ ,  $0.35R$ ,  $0.60R$ ,  $0.82R$ , and  $0.92R$ , respectively, where  $R$  denotes the blade radius. According to the MEXICO experiment, the zero rotor azimuthal angle is defined as the 12 o'clock position (pointing upward) for blade 1. Moreover, the upwind and downwind sides of the rotor plane are the 9 o'clock and 3 o'clock positions, respectively.

Figures 18 and 19 display azimuthal variation of the tangential and normal forces at  $0.25R$  and  $0.35R$  of blade 1. The potential solution and the measurement data show almost the same trend although the VLFW method overpredicts the tangential force about 20% and 75% at  $0.25R$  and  $0.35R$ , respectively, about 50% and 35% at  $0.25R$  and  $0.35R$ , respectively, for the normal force, respectively. The viscous solution makes a slight improvement in terms of magnitude of the tangential and normal forces; however, it cannot predict the extrema, especially for the tangential force. This implies that the viscous effects (separated flow and stall condition) are not well captured by the viscous solution in the blade root region. Moreover, it is expected that the dynamic stall solution makes adjustment between the potential and viscous solutions in terms of the force magnitude and phasing. But, it seems that it makes a slight improvement only for the blade root region (inboard positions), especially for the tangential forces.

Azimuthal variation of the tangential and normal forces at  $0.6R$  of the blade 1 is presented in Fig. 20. Despite a rather good trend between different methods and the experiment, there is an

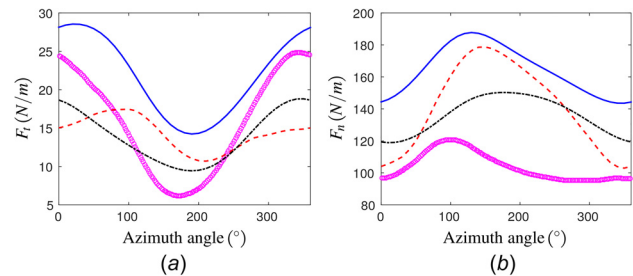


**Fig. 18** Azimuthal variation of (a) tangential and (b) normal forces at  $0.25R$  of radial position, MEXICO turbine, yawed flow, case 1, — potential, -- viscous, - - - dynamic stall, and  $\circ$  experiment

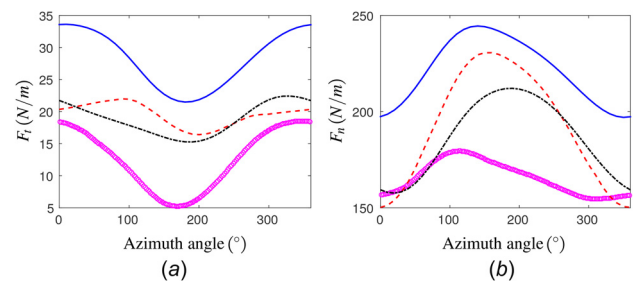


**Fig. 19** Azimuthal variation of (a) tangential and (b) normal forces at  $0.35R$  of radial position, MEXICO turbine, yawed flow, case 1, — potential, -- viscous, - - - dynamic stall, and  $\circ$  experiment

overprediction of approximately 40% and 30% for the tangential and normal forces, respectively. The same tendency between the curves implies that the flow is attached to the blade surface in the midboard region (no separation). Nevertheless, the large offset between the simulation and the measurement may be explained

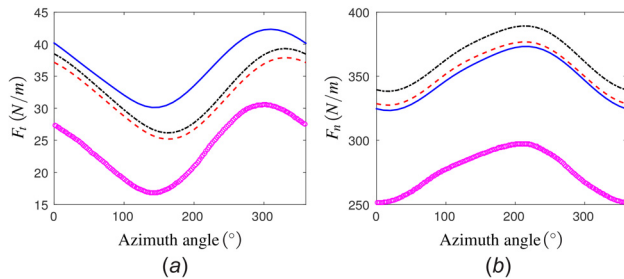


**Fig. 20** Azimuthal variation of (a) tangential and (b) normal forces at  $0.60R$  of radial position, MEXICO turbine, yawed flow, case 1, — potential, -- viscous, - - - dynamic stall, and  $\circ$  experiment

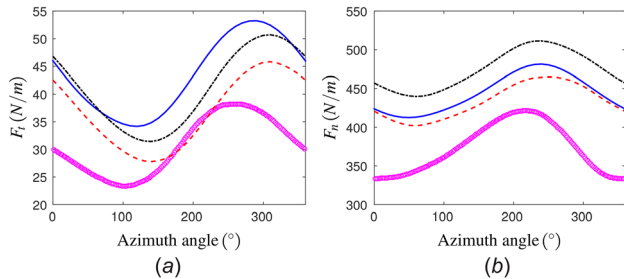


**Fig. 21** Azimuthal variation of (a) tangential and (b) normal forces at  $0.82R$  of radial position, MEXICO turbine, yawed flow, case 1, — potential, -- viscous, - - - dynamic stall, and  $\circ$  experiment

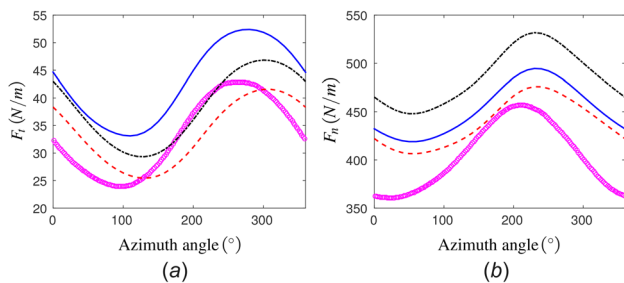


**Fig. 22** Azimuthal variation of (a) tangential and (b) normal forces at  $0.92R$  of radial position, MEXICO turbine, yawed flow, case 1, — potential, -- viscous, - - - dynamic stall, and  $\circ$  experiment

due to the poor quality of the interpolated airfoil profile at  $0.6R$  located at the transition region between the Risø and NACA airfoils (see Fig. 15).

Figures 21 and 22 show the tangential and normal forces at  $0.82R$  and  $0.92R$  of the blade 1 as a function of azimuthal angle. Apart from a qualitative agreement between the simulations and measurements, as discussed in the previous paragraph, the same tendency between the different methods and experiments reveals that the flow over the outboard region of the blade 1 is not separated. Moreover, a significant phase shift between the simulation and measurement is observed where the simulations predict the later maximum peak than the measurement. Finally, the adjustment role of the dynamic stall model between the potential and viscous solutions is noticeable for the tangential force.

## 5 Conclusions

A time-marching vortex lattice free wake is used for the prediction of aerodynamic loads on rotor blades. It is based on the

inviscid, incompressible, and irrotational flow (potential flow) where its potential solution is coupled to the tabulated airfoil data and a semi-empirical model to take into account the viscosity and the dynamic stall effects, respectively. Three different methods called the standard potential method, the 2D static airfoil data method, and the dynamic stall method are introduced and they are compared with the BEM method and the GENUVP code.

The results show that for more accurate load and power prediction, coupling to the 2D static airfoil data is necessary even though some complex conditions such as separated flow, stall condition, and centrifugal forces cannot be well predicted.

Furthermore, the predicted forces using the dynamic stall solution do not make considerable improvements with respect to the other load calculation methods. This may be because of the several airfoil-dependent coefficients used in the extended ONERA model while in case of no wind tunnel measurements they are taken from the flat plate and mean airfoil.

The predicted power production by different methods for the NREL 5-MW turbine shows that the potential, inviscid, and irrotational assumptions of the vortex flow are relevant to a broad range of operating conditions. The VLFW method predicts higher normal and tangential forces compared with the MEXICO experiment. For the normal forces, the maximum peak occurs downwind of the rotor plane whereas it occurs upwind of the rotor plane when moving from inboard sections toward the outboard sections. The difference between the maximum peak positions along the rotor blade with respect to the rotor plane induces an additional moment on the rotor due to the yaw misalignment. Furthermore, for almost all spanwise sections, the simulation presents a phase shift against the experiments for both the normal and tangential forces; nevertheless, it predicts the azimuthal load variation rather well.

A considerable discrepancy between the simulations and measurement data for the MEXICO turbine close to the blade root (inboard sections) may be physically explained due to the thick airfoil profiles which consequently results in the flow separation and stall condition even if at lower wind velocities. This is also certified for the NREL 5-MW machine.

According to Refs. [28,29], a deficiency in the streamwise velocity (around 1 m/s) due to open type wind tunnel employed in the experimental investigation has been reported. It is expected that the predicted forces by the VLFW simulation are slightly improved by taking the tunnel effect into account.

## Acknowledgment

The technical support of National Technical University of Athens (NTUA) to use the GENUVP is gratefully acknowledged. (GENUVP is an unsteady flow solver based on vortex blob approximations developed for rotor systems by National Technical University of Athens).

The data used have been supplied by the consortium which carried out the EU FP5 project MEXICO: "Model rotor EXperiments in Controlled conditions."

This work was financed through the Swedish Wind Power Technology Centre (SWPTC). SWPTC is a research center for the design and production of wind turbines. The purpose of the center is to support Swedish industry with knowledge of design techniques and maintenance in the field of wind power. The work is carried out in six theme groups and is funded by the Swedish Energy Agency and by academic and industrial partners.

## Appendix: Extended ONERA Model

The extended ONERA model is used to predict the unsteady lift, drag, and moment coefficients based on 2D static airfoil data. In the initial version of the ONERA model, the excitation variable

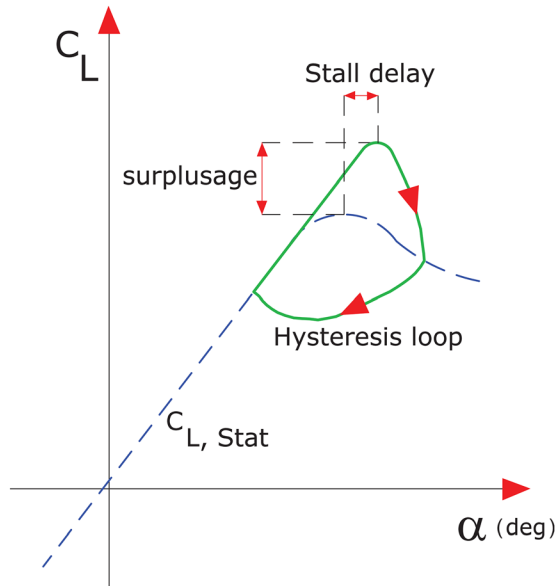


Fig. 23 Hysteresis loop around the stall angle

is the angle of attack with respect to the chord line whereas in the extended version, the excitation variables are  $W_0$  and  $W_1$ , the velocity component perpendicular to the sectional chord and the blade element angular velocity for the pitching oscillation, respectively. Furthermore, compared with the initial version of the ONERA model, in the extended model, instead of the lift coefficient ( $C_L$ ), the circulation ( $\Gamma$ ) which is responsible for producing lift is the response variable. Also, the variation of the wind velocity is included in the extended model which does not exist in the early version [17].

In steady flow, when the angle of attack for some blade regions exceeds from the critical angle of attack ( $\alpha_{stall}$ ), which is equivalent to the maximum lift coefficient ( $C_{L,max}$ ), the flow is separated. This phenomenon is called static stall. This phenomenon, for an airfoil in an unsteady flow, is associated with so-called dynamic stall where its major effect is stall delay and an excessive force (see Fig. 23). In other words, when an airfoil or a lifting surface is exposed to time-varying pitching, plunging and incident velocity, the stall condition happens at an angle of attack higher than the static stall angle which means that the flow separates at a higher angle of attack than in steady flow. When stall occurs, there is a sudden decrease in lift. By decreasing the angle of attack, the flow reattaches again (stall recovery), but at a lower angle than the static stall angle [30]. This scenario, which is called dynamic stall, occurs around the stall angle and the result is hysteresis loops and a sudden decrease of the lift coefficient. Hence, the dynamic stall describes a series of event resulting in dynamic delay of stall to angles above the static stall angle and it provides the unsteady evolution of lift, drag, and moment coefficients along the rotor blade.

In Eqs. (22) and (23),  $S_L$ ,  $K_L$ , and  $\sigma_D$  are airfoil dependent coefficients. However, in case of no wind tunnel measurement data, the flat plate values are applied as  $S_L = \pi$  and  $K_L = \pi/2$  for small Mach number. The term  $\sigma_D$  is expressed by

$$\sigma_D = \sigma_{0D}\alpha + \sigma_{1D}|\Delta C_L| \quad (A1)$$

where for the flat plate,  $\sigma_{0D} = 0$  and  $\sigma_{1D} = 0$ . Moreover,  $\Delta C_L = C_{L, Lin} - C_{L, Stat}$  where the Lin and Stat subscripts represent the linear region and the static condition, respectively (see Figs. 24 and 25). The linear circulation concerning the attached flow lift ( $\Gamma_{1L}$ ) is calculated by the first-order differential equation as

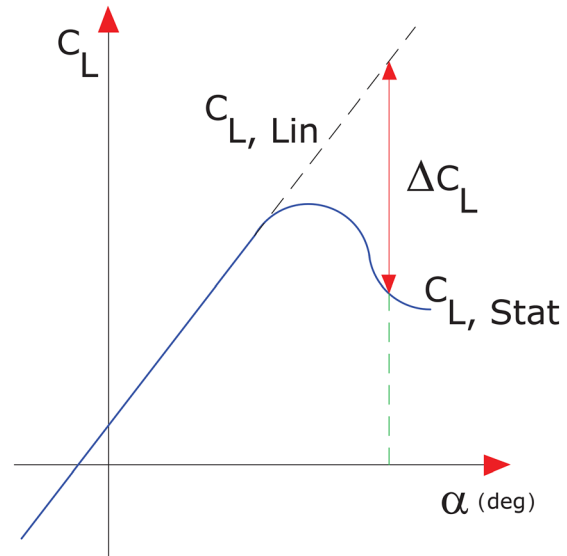


Fig. 24 Definition of the lift coefficient parameters in the ONERA model

$$\begin{aligned} \dot{\Gamma}_{1L} + \lambda_L \frac{2V_p}{c} \Gamma_{1L} \\ = \lambda_L \frac{2V_p}{c} \left( \frac{dC_L}{d\alpha} \right)_{Lin} (W_0 - V_p \alpha_0) + \lambda_L \frac{2V_p}{c} \sigma_L W_1 \\ + \left( \alpha_L \left( \frac{dC_L}{d\alpha} \right)_{Lin} + d_L \right) \dot{W}_0 + \alpha_L \sigma_L \dot{W}_1 \end{aligned} \quad (A2)$$

where  $V_p$ ,  $dC_L/d\alpha$ , and  $\alpha_0$  are the total velocity component parallel to the airfoil chord, slope of the  $C_L$  versus  $\alpha$  curve in the linear region and the zero-lift angle of attack of each blade element, respectively.

The nonlinear circulation concerning the stall correction of lift ( $\Gamma_{2L}$ ) is calculated by the second-order differential equation as

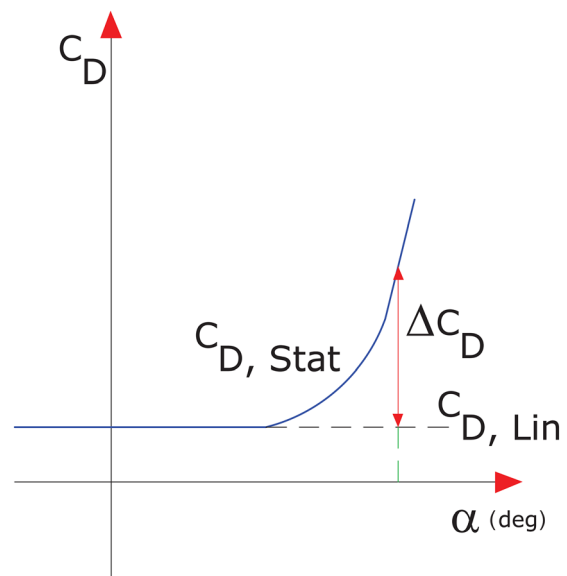


Fig. 25 Definition of the drag coefficient parameters in the ONERA model

$$\begin{aligned} \ddot{\Gamma}_{2L} + a_L \frac{2V_p}{c} \dot{\Gamma}_{2L} + r_L \left( \frac{2V_p}{c} \right)^2 \Gamma_{2L} \\ = -r_L \left( \frac{2V_p}{c} \right)^2 V_p \Delta C_L - e_L \frac{2V_p}{c} \dot{W}_0 \end{aligned} \quad (A3)$$

Furthermore, the nonlinear circulation concerning the stall correction of drag ( $\Gamma_{2L}$ ) is given by the second-order differential equation as

$$\begin{aligned} \ddot{\Gamma}_{2D} + a_D \frac{2V}{c} \dot{\Gamma}_{2D} + r_D \left( \frac{2V}{c} \right)^2 \Gamma_{2D} \\ = -r_D \left( \frac{2V}{c} \right)^2 V \Delta C_D - e_D \frac{2V}{c} \dot{W}_0 \end{aligned} \quad (A4)$$

In Eqs. (22), (A2), (A3) and (A4), the symbol  $(\dot{\quad})$  denotes the derivation with respect to time.

In the above equations,  $\lambda_L$ ,  $\sigma_L$ , and  $\alpha_L$  depend on the specific airfoil type and they must be determined from experimental measurements. If experimental data for a particular airfoil are not available, these coefficients take the flat plate values as  $\lambda_L = 0.17$ ,  $\sigma_L = 2\pi$ ,  $\alpha_L = 0.53$ .  $d_L$  in Eq. (A2) and the coefficients in Eqs. (A3) and (A4) are functions of  $\Delta C_L$  due to the flow separation and they are defined as

$$\begin{aligned} d_L &= \sigma_L |\Delta C_L| \\ a_L &= a_{0L} + a_{2L} (\Delta C_L)^2 \\ a_D &= a_{0D} + a_{2D} (\Delta C_L)^2 \\ \sqrt{r_L} &= r_{0L} + r_{2L} (\Delta C_L)^2 \\ \sqrt{r_D} &= r_{0D} + r_{2D} (\Delta C_L)^2 \\ e_L &= e_{2L} (\Delta C_L)^2 \\ e_D &= e_{2D} (\Delta C_L)^2 \end{aligned} \quad (A5)$$

The coefficients in Eq. (A5) are airfoil dependent. In case of no wind tunnel measurements, the values for a mean airfoil may be taken and the flat plate values cannot be used. For the mean airfoil,  $\sigma_{1L} = 0.0$ ,  $a_{0L} = 0.1$ ,  $a_{2L} = 0.0$ ,  $r_{0L} = 0.1$ ,  $r_{2L} = 0.0$ ,  $e_{2L} = 0.0$ ,  $a_{0D} = 0.0$ ,  $a_{2D} = 0.0$ ,  $r_{0D} = 0.1$ ,  $r_{2D} = 0.0$ , and  $e_{2D} = 0.0$ .

## References

- [1] Hansen, M. O., 2008, *Aerodynamics of Wind Turbines*, 2nd ed., EarthScan, London.
- [2] van Garrel, A., 2003, "Development of a Wind Turbine Aerodynamics Simulation Module," Energy Research Centre of the Netherlands (ECN), Petten, The Netherlands, Report No. ECN-C-03-079.
- [3] Vermeer, L., Sørensen, J., and Crespo, A., 2003, "Wind Turbine Wake Aerodynamics," *Prog. Aerosp. Sci.*, **39**(6–7), pp. 467–510.
- [4] Opoku, D. G., Triantos, D. G., Nitzsche, F., and Voutsinas, S. G., 2002, "Rotorcraft Aerodynamic and Aeroacoustic Modeling Using Vortex Particle Methods," 23rd International Congress of the Aeronautical Sciences (ICAS), Toronto, ON, Canada, Sept. 8–13, Paper No. ICAS 2002-2.1.3.
- [5] Voutsinas, S. G., Beleiss, M. A., and Rados, K. G., 1995, "Investigation of the Yawed Operation of Wind Turbines by Means of a Vortex Particle Method," *AGARD Conference Proceedings*, Vol. 552, pp. 11.1–11.
- [6] Zhao, J., and He, C., 2010, "A Viscous Vortex Particle Model for Rotor Wake and Interference Analysis," *J. Am. Helicopter Soc.*, **55**(1), p. 12007.
- [7] Egoft, T. A., 1988, "Helicopter Free Wake Prediction of Complex Wake Structures Under Blade-Vortex Interaction Operating Conditions," 44th Annual Forum of the American Helicopter Society, Washington, DC, June 16–18, pp. 819–832.
- [8] Rosen, A., and Graber, A., 1988, "Free Wake Model of Hovering Rotors Having Straight or Curved Blades," *J. Am. Helicopter Soc.*, **33**(3), pp. 11–21.
- [9] Bagai, A., 1995, "Contribution to the Mathematical Modeling of Rotor Flow-Fields Using a Pseudo-Implicit Free Wake Analysis," Ph.D. thesis, University of Maryland, College Park, MD.
- [10] Gupta, S., 2006, "Development of a Time-Accurate Viscous Lagrangian Vortex Wake Model for Wind Turbine Applications," Ph.D. thesis, University of Maryland, College Park, MD.
- [11] Pasmajoglou, S., and Graham, J., 2000, "Prediction of Aerodynamic Forces on Horizontal Axis Wind Turbines in Free Yaw and Turbulence," *J. Wind Eng. Ind. Aerodyn.*, **86**(1), pp. 1–14.
- [12] Voutsinas, S., 2006, "Vortex Methods in Aeronautics: How To Make Things Work," *Int. J. Comput. Fluid Dyn.*, **20**(1), pp. 3–18.
- [13] Chattot, J., 2007, "Helicoidal Vortex Model For Wind Turbine Aeroelastic Simulation," *Comput. Struct.*, **85**(11–14), pp. 1072–1079.
- [14] Chattot, J., 2003, "Optimization of Wind Turbines Using Helicoidal Vortex Model," *ASME J. Sol. Energy Eng.*, **125**(4), pp. 418–424.
- [15] Holierhoek, J., de Vaal, J., van Zuijlen, A., and Bijl, H., 2013, "Comparing Different Dynamic Stall Models," *J. Wind Energy*, **16**(1), pp. 139–158.
- [16] Leishman, J., 2002, "Challenges in Modeling the Unsteady Aerodynamics of Wind Turbines," *AIAA Paper No. 2002-0037*.
- [17] Bierbooms, W., 1992, "A Comparison Between Unsteady Aerodynamic Models," *J. Wind Eng. Ind. Aerodyn.*, **39**(1–3), pp. 23–33.
- [18] Schepers, J., and Boorsma, K., 2006, "Description of Experimental Setup MEXICO Measurements," Energy Research Centre of the Netherlands (ECN), Petten, The Netherlands, Report No. ECN-X-09-0XX.
- [19] Anderson, J., 2001, *Fundamentals of Aerodynamics*, 3rd ed., McGraw-Hill, New York.
- [20] van Garrel, A., 2001, "Requirements for a Wind Turbine Aerodynamics Simulation Module," 1st ed., Energy Research Centre of the Netherlands (ECN), Petten, The Netherlands, Report No. ECN-C-01-099.
- [21] Leishman, J., and Bagai, M. J., 2002, "Free Vortex Filament Methods for the Analysis of Helicopter Rotor Wakes," *J. Aircr.*, **39**(5), pp. 759–775.
- [22] Bhagwat, M., and Leishman, J., 2002, "Generalized Viscous Vortex Model for Application to Free-Vortex Wake and Aeroacoustic Calculations," 58th Annual Forum and Technology Display of the American Helicopter Society International, Montreal, Canada, June 11–13, pp. 2042–2057.
- [23] Vassitas, G., Kozel, V., and Mih, W., 1991, "A Simpler Model for Concentrated Vortices," *Exp. Fluids*, **11**(1), pp. 73–76.
- [24] Bagai, A., and Leishman, J., 1993, "Flow Visualization of Compressible Vortex Structures Using Density Gradient Techniques," *Exp. Fluids*, **15**(6), pp. 431–442.
- [25] Katz, J., and Plotkin, A., 2001, *Low-Speed Aerodynamics*, 2nd ed., Cambridge University Press, New York.
- [26] Jonkman, J., Butterfield, S., Musial, W., and Scott, G., 2009, "Definition of a 5-MW Reference Wind Turbine for Offshore System Development," National Renewable Energy Laboratory, Golden, CO, Report No. NREL/TP-500-38060.
- [27] Abedi, H., 2013, "Development of Vortex Filament Method for Aerodynamic Loads on Rotor Blades," *Licentiate thesis*, Chalmers University of Technology, Gothenburg, Sweden.
- [28] Chasapogiannis, P., and Voutsinas, S., 2014, "Aerodynamic Simulations of the Flow Around a Horizontal Axis Wind Turbine Using the GAST Software," National Technical University of Athens, Athens, Greece, Ref. No. 68/1110 (in Greek).
- [29] Abedi, H., Davidson, L., and Voutsinas, S., 2015, "Numerical Studies of the Upstream Flow Field Around a Horizontal Axis Wind Turbine," *AIAA Paper No. 2015-0495*.
- [30] Reddy, T. S. R., and Kaza, K. R. V., 1989, "Analysis of an Unswept Propfan Blade With a Semi Empirical Dynamic Stall Model," NASA Lewis Research Center, Cleveland, OH, Report No. NASA-TM-4083.